Raport ştiinţific sintetic final

privind implementarea proiectului PN-III-P4-ID-PCE-2016-0649 - 194/2017 cu titlul "Parallel theoretical study of the two components of the prompt fission neutrons: dynamically released at scission (SN) and evaporated from fully accelerated fragments (EVN)" în perioada august 2017 - decembrie 2019

1 Phase nr. 1 (09/08/2017 - 20/12/2017)

The shape of the energy spectrum of neutrons emitted during scission.

1.1 Estimated results

The evolution of the impulse distribution and of the energy spectrum of the scission neutrons during their separation from the fissionable nucleus.

It is expected that the scission neutron spectrum differs from the evaporated neutron spectrum at very low and very high energies.

1.2 Activities

The Fourier transform calculation of single particle wave functions in spherical and deformed nuclei. The deduction of corresponding impulse distributions.

1.3 Introduction

The goal of the project is to provide elements for answering the important question of the nature and relative abundance of the two components of prompt fission neutrons (PFN): released at scission and evaporated from fully accelerated fragments.

We have used a dynamical scission model to estimate the main properties of the scission neutrons (SN), based on the solution of the time-dependent Schrödinger equation [1], [2]. When the calculated data have been compared with measurements of PFN during 235U(n_{th},f) the experimental trends are well reproduced. Based on this evidence, one cannot decide anymore which is the main source of PFN. It is therefore necessary to extend the application of our model to other observables and other fissioning systems to see how far this agreement holds. Also, the same quantities will be calculated with both models (scission and evaporation) to decide which is more realistic.

In this phase we have determined the energy spectrum of the SN. For this we have calculated the Fourier transforms (FT) of the unbound parts of the wave packets that

describe the SN immediately after scission. These provides the SN momentum distribution from which one can derive the kinetic energy distribution. It is expected that at low and high kinetic energies the SN spectrum differs from the evaporation spectrum leading to an opportunity to distinguish between the two components of the PFN.

To make possible the treatment of both spherical and deformed nuclei, we have developed adequate numerical procedures to calculate the FT of a WF in cylindrical coordinates.

1.4 Formalism

1.4.1 Fourier transform

The standard form of the Fourier transform of a function $\Psi(\vec{r})$ in three dimensions is:

$$\Phi(\vec{k}) = \frac{1}{(2\pi)^{3/2}} \int_{-\infty}^{\infty} \Psi(\vec{r}) \mathrm{e}^{-\mathrm{i}\vec{k}\vec{r}} \mathrm{d}^3\vec{r}, \qquad \vec{k} = \vec{p}/\hbar. \tag{1}$$

It gives the probability in the momentum space i.e., the probability that the nucleon has its momentum $\vec{p}$ in the volume element $\mathrm{d}^3\vec{p}$.

In our applications we consider nuclear forms with axial symmetry so that we use the cylindrical coordinates (ρ, z) and omit the dependence on the angle θ. It can be shown that the Fourier transform in this case has the form:

$$F(R, Z) = 2\pi \int_{-\infty}^{\infty} \left[\int_{0}^{\infty} f(\rho, z) J_0(2\pi\rho R) \rho \mathrm{d}\rho \right] \mathrm{e}^{-2\pi \mathrm{i} z Z} \mathrm{d}z \tag{2}$$

where J_0 is the zero-order Bessel function of the first kind. The transform with respect to the variables ρ, R is called the zero-order Hankel transform. The form used in quantum mechanics is based to the relations $R = k_\rho/(2\pi)$ and $Z = k_z/(2\pi)$. The variables ρ, z belong to the position space, while k_ρ, k_z belong to the momentum space. The factor $1/2\pi$ is introduced as a phase convention. Suppose now that the function $f(\rho, z)$ is known only on the nodes of a discrete grid. Then, the Fourier transform will be also a discrete function, approximation of the continuous transform. Let $\rho_j = \rho_0 + j\Delta\rho,\ j = 0, 1, \ldots, M-1$ and $z_k = z_0 + k\Delta z,\ k = 0, 1, \ldots, N-1$ be the points (uniformly spaced) defining the grid for which $f(\rho_j, z_k)$ are given. The Fourier transform will be also calculated on a grid with the mesh points R_m, Z_n. The Hankel transformation is performed by a quadrature formula (see [3]) whose coefficients are expressed in terms of Bessel and Struve functions, while the discrete Fourier transform is calculated by the Fast Fourier Transform - FFT [4].

1.4.2 Time dependent wave functions

They are solutions of the time dependent Schrödinger equation (TDSE) with time dependent potential (TDP):

$$i\hbar \frac{\partial \Psi(\rho, z, t)}{\partial t} = \mathcal{H}(\rho, z, t) \Psi(\rho, z, t), \tag{3}$$

$$\mathcal{H}\Psi = \begin{bmatrix} O_1 - CS_c & -CS_a \\ -CS_b & O_2 - CS_d \end{bmatrix} \begin{bmatrix} f^{(1)} \\ f^{(2)} \end{bmatrix}, \tag{4}$$

$$O_{1,2} = -\frac{\hbar^2}{2\mu}(\Delta - \frac{\Lambda_{1,2}^2}{\rho^2}) + V(\rho, z, t).$$

Δ is the Laplacean, V is the potential, C is a constant and the operators $S_a, \ldots, S_d$ represent the spin-orbit coupling.

1.5 Dynamical scission model

We use the solution of the TDSE to study the time evolution of the neutron states in a nucleus that undergoes scission. We separate the calculation in two stages:

1)The scission process itself, i.e., the neck rupture and its absorption by the fragments. The corresponding nuclear configurations are defined by a set of deformations $\{\alpha_i\}$ (just before scission) and $\{\alpha_f\}$ (immediately after scission). The duration of this stage is relatively short ($\Delta T \approx 10^{-22}$ sec) and the potential in which the neutrons move changes rapidly.

2)The detachment from the fragments of the fraction of the neutrons that are left unbound at the end of the previous stage. Since, at this stage, their motion is much faster than that of the just separated fragments we freeze, in a first approximation, the fragments at the configuration $\{\alpha_f\}$ and keep the potential constant during this stage.

1.5.1 Physical quantities

We follow the motion of the wave packet that describes the unbound neutrons in time and calculate quantities like:

• The probability that a neutron occupying the state $|\Psi^i\rangle$ before scission populates a state $|\Psi^f\rangle$ after a time interval T: $a_{if} = \langle\Psi^i(T)|\Psi^f\rangle = 2\pi \int\int \rho\Psi^i(T)\Psi^f d\rho dz$.

• The probability that the neutron is emitted, given by: $P_{em}^i = v_i^2(\sum_{unbound} |a_{if}|^2) = v_i^2(1 - \sum_{bound} |a_{if}|^2)$ where v_i^2 are the occupation probabilities of the initial eigenstates.

• The emitted part of the wave packet: $|\Psi_{em}^i\rangle = |\Psi^i(T)\rangle - \sum_{bound} a_{if}|\Psi^f\rangle$.

From the emitted wave function one can deduce important characteristics of the process as: the spatial distribution of the emission points, the current density, the angular distribution and the total number of emitted neutrons.

In the following we present the evolution of the Fourier transform and of the momentum distribution for some emitted wave functions.

1.6 The evolution of the emitted wave functions and of the momentum distributions; the energy spectrum

We have investigated the reaction $^{235}U(n_{th}, f)$ with the light fragment mass $A_L = 96$ (which is the most probable experimental mass asymmetry). Two parameters of the Cassini representation have been considered: α (elongation) and α_1 (mass asymmetry). We have chosen: $\alpha = 0.985$ (before scission) and $\alpha = 1.001$ (after scission). The parameter α_1 results from the condition of fixed ratio of the fragment volumes that corresponds to A_L=96. We have performed the Fourier transform for several wavefunctions corresponding to $\Omega = 1/2$. At each point in the (k_ρ, k_z) plane are associated an absolute value $K = \sqrt{k_\rho^2 + k_z^2}$ and a probability $P = |F(k_\rho, k_z)|^2 k_\rho \Delta k_\rho \Delta k_z$. To represent the K-distributions as histograms, we divide the domain of K-values in equal intervals and group the points according to the interval to which they belong. Summing up the probabilities of the points in each group one obtains the probability $P(K)$ that a neutron has its K-value in the respective interval. In the figures 1 and 2 are shown the emitted wavefunctions with the indices 30 and 33 (as sum of square moduli of the two components) aside with the momentum histograms at different times T. The time-dependent wavefunctions are represented relative to the function at $T = 20$, while the values on the ordinates of the histograms are the $P(K)$ probabilities multiplied by 10^2.

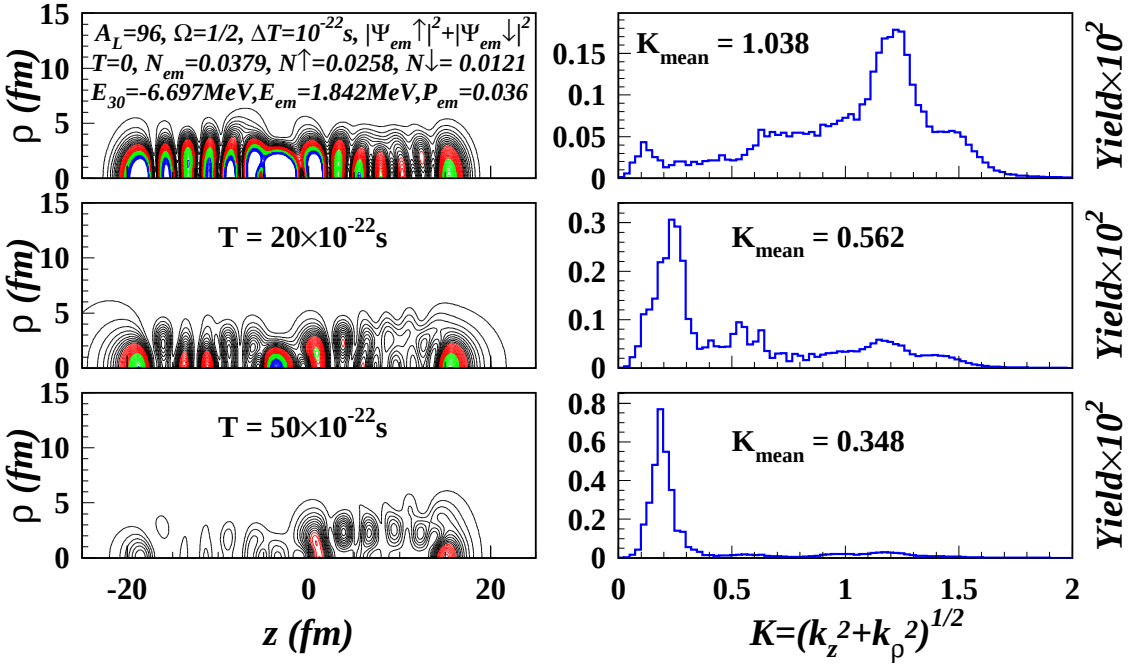

Figure 1: Square modulus of the emitted WF_{30} and momentum distribution at different times T. N_{em} is the norm of the emitted function, N↑, N↓ are the norms of the two components and $K_{mean} = \frac{\sum_{m,n} KP}{\sum_{m,n} P}$, $P = k_\rho |F|^2 dk_\rho dk_z$.

As one can see, at increasing time intervals the wavefunction values are diminishing, showing that the neutron is leaving the nucleus. At the same time, the K-distributions

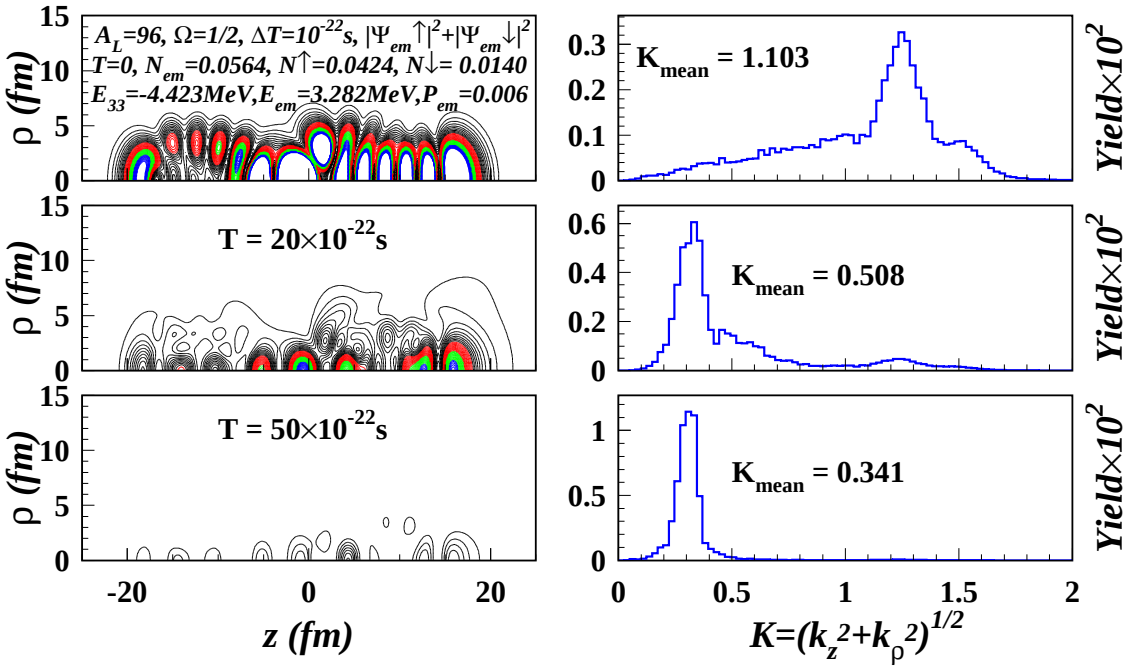

Figure 2: The same as in Fig.1 but for the emitted WF_{33}.

are shrinked to lower values, reflecting the fact that the neutrons are less and less present in the potential well. At large times they tend to a gaussian shape.

From the momentum distribution one can deduce the kinetic energy distribution (according to $E = \frac{\hbar^2}{2\mu}K^2$). To obtain the whole kinetic energy spectrum one has to repeat such calculations for all the states at each Ω value. Here we present results only for Ω=1/2 states and from WF_{11} to WF_{41}. The states lying at the bottom of the well (WF_1 to WF_{10}) have negligible P_{em} values. Note however that $\Omega = 1/2$ gives the dominant contribution (65%).

Fig. 3 shows kinetic energy spectra for two individual states (30 and 33) around the Fermi level and the sum for all Ω=1/2 states with the index above 10 (having energies greater than -23 MeV). The total spectrum presents a maximum around 0.7 MeV and an exponentially decreasing tail till 5 MeV in qualitative agreement with the measured spectrum [5] of all prompt fission neutrons (PFN).

In the Fig.4 the total energy spectrum (summed over Ω values from 1/2 to 9/2) is given as histogram. For comparison, we added recent data [6] obtained for the same constraint on mass asymmetry ($A_L = 96$). The calculated histogram is normalized to these data, the factor being 2.52/0.51 i.e., the ratio between the PFN multiplicity measured for the most probable mass division (A_L=96) [7] and the number of neutrons that are outside the nucleus at $T = 50 \times 10^{-22}$ sec.

Two typical evaporation spectra [8], $E\exp(-E/Temp)$, characterized by nuclear temperatures $Temp = 1.0$ and 0.9 MeV are also plotted for comparison. The evaporation spectra follow quite well the general trend of the recent data except at very low and

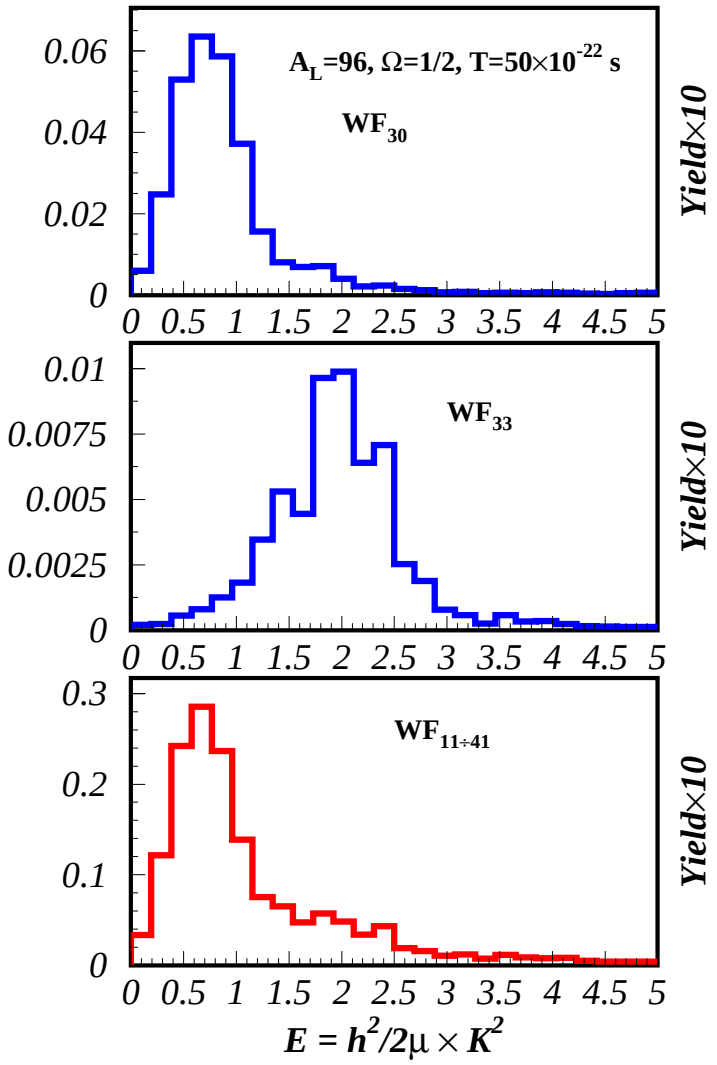

Figure 3: Energy distribution at T= 50×10^{-22} sec (Yield = $P(K) \times v_i^2$).

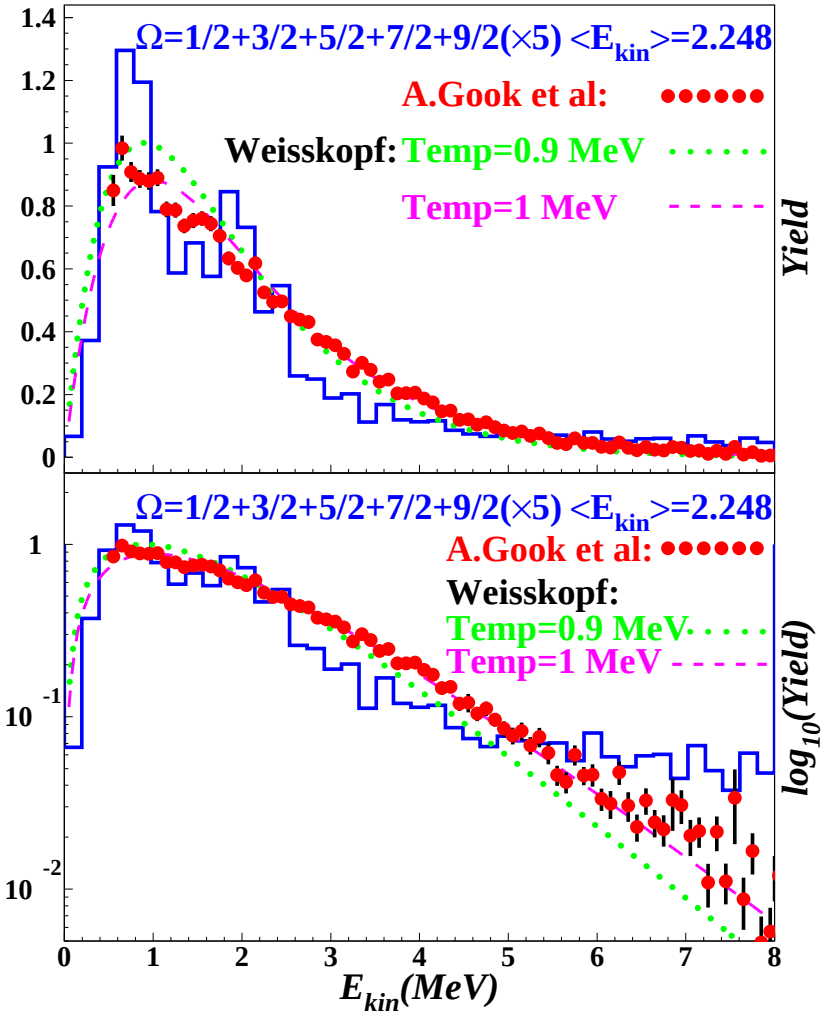

Figure 4: Kinetic energy distributions at $T = 50 \times 10^{-22}$ sec calculated with all neutron states together with recent experimental results [6] from the reaction $^{235}U(n_{th}, f)$. $Yield = \sum P_i(E_{kin}) \times v_i^2$.

very high energies. One notices that both the data and the calculation are not smooth. The oscillations in the data are statistically significant. The calculated distribution is not smooth since it consists of a finite weighted sum of individual contributions with different mean values and widths.

In the lowest frame the same comparison is shown in lin-log scale to unveil hidden differences at $E_{kin} > 5$ MeV. One can see that the SN can reproduce the high energy tail of the PFN spectrum.

1.7 Conclusions

In this phase we have presented numerical procedures to calculate the Fourier transform on wave functions given in cylindrical coordinates and applications to the study of scission neutrons. As initial functions for our procedure we have taken single-particle states in extremely deformed nuclei associated with the wave packets of the neutrons released during scission. We propagate the neutron wave packets in time through the bi-dimensional TDSE with TDP. We calculate the Fourier transforms at different times T for different Ω states and the momentum distributions corresponding to these transforms. From such distributions one can follow the separation of the neutron from the fissioning system and obtain the kinetic energy spectrum of each emitted neutron. The shape of the energy spectrum obtained summing over all emitted neutrons resembles the measured PFN spectrum.

2 Phase nr. 2 (21/12/2017 - 20/12/2018)

The calculus of the time dependence of the decay rate. The dependence of the energy spectrum and of the angular distribution of the scission neutrons on the quantum number Ω.

2.1 Estimated results

This calculation will reveal the dynamics of the emission process. It will be established how long it takes before 10%, 50% and 90% of neutrons leave the fissioning nucleus. The evaluation of the relative contribution of each set of neutron eigenstates (Ω) to these distributions.

2.2 Activities

The study of the competition between the two components of the prompt fission neutrons in the region where the evaporated (EVN) and the scission neutrons (SN) overlap - Part I.

The establishment of the character of the emission process of the scission neutrons: exponential or oscillatory? By knowing the energy and the angular domain at which each set contributes one can select experimentally the neutrons with well defined quantum numbers.

2.3 Introduction

In this phase we have determined the time dependent decay rate for the neutrons leaving a sphere around the nucleus. This provides additional informations about the evolution of the emission process. Thus, it has been evaluated the time necessary for different amount of neutrons to be released from the fissioning nucleus and it was shown the character of the SN emission (exponential or oscillatory). The dependence of the decay rate on the quantum number Ω and on the radius of the sphere around the nucleus was also studied. The scission-neutron angular distribution and the energy spectrum have been calculated for different time intervals and for several Ω values as well.

2.4 The decay rate

Let $\Psi(\rho, z, t)$ be the solution of the time dependent Schrödinger equation. One defines **the total escape probability** as the fraction of the wave function located beyond a shere of radius R around the nucleus at the time t:

$$P_{tun}(t) = 2\pi \int_{D_{ext}} |\Psi(\rho, z, t)|^2 \rho d\rho dz. \tag{5}$$

The total decay rate is related to the total escape probability by

$$\lambda(t) = \frac{1}{N_{tot} - P_{tun}} \frac{dP_{tun}(t)}{dt} \tag{6}$$

where N_{tot} is the total norm given by

$$N_{tot}(t) = 2\pi \int_{D} |\Psi(\rho, z, t)|^2 \rho d\rho dz. \tag{7}$$

The infinite total domain D is limited in calculations to a finite one by the numerical boundaries. In practice, $N_{tot} - P_{tun}$ is replaced by

$$N_{int}(t) = 2\pi \int_{D_{int}} |\Psi(\rho, z, t)|^2 \rho d\rho dz \tag{8}$$

which is more convenient for calculations. The domain D_{int} is delimited by the semicircle of radius R, while the domain D_{ext} is the complementary of D_{int} with respect to D.

To calculate dP_{tun}/dt, instead of a low accurate numerical derivative, we made use of **the continuity equation**:

$$\frac{\partial p}{\partial t} + \nabla J = 0 \tag{9}$$

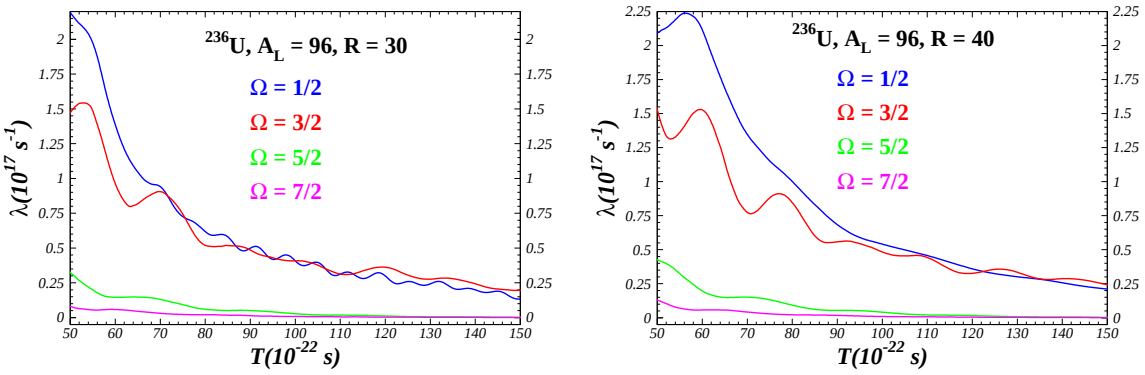

Figure 5: Scission-neutron decay rates as functions of time calculated on spheres of radius R=30 fm (left) and R=40 fm (right) with sets of neutron wavefunctions characterized by a given quantum number Ω.

where $p(r,t) = |f(r,t)|^2$ is **the probability density** (r being the spatial coordinate vector and f being the solution of TDSE), while $J(r,t)$ is the **the current density**. According to the continuity equation, we have:

$$\frac{dP_{tun}(t)}{dt} = \frac{d}{dt}\left(2\pi \int_{D_{ext}} |f(\rho,z,t)|^2 \rho d\rho dz\right) = -2\pi \int_{D_{ext}} \nabla J \rho d\rho dz$$

Tacking the expression of ∇J in cylindrical coordinates one arrives to a sum of double integrals. These double integrals are transformed into curvilinear integrals, according to the Green formula. Thus, enough accurate value of the decay rate can be obtained.

We have investigated the reaction $^{235}U(n_{th}, f)$ with the light fragment mass $A_L = 96$.

Fig.5 shows the time-dependent decay rate for 2 values of the radius R (30 and 40 fm) of the sphere that separates the external from the internal domain. The results are presented separately for sets of neutron wave functions characterized by a given value of the quantum number Ω. One can see that $\lambda(t)$ has an oscillatory behaviour immediately after the neck rupture. With increasing time the amplitude of these oscillations diminishes and asymptotically reaches an almost constant value indicative of an exponential decay. This feature is more visible at high Ω values (5/2 and 7/2) where there is a centrifugal barrier to be tunneled. Fig.6 shows the comparison of the time dependent decay rate for the two values of the radius R. One sees that although the neutron flux needs longer time to reach the larger sphere, asymptotically they tend to the same value. This result constitutes a validity test of our calculations.

Table 1 shows how long it takes for scission neutrons with different Ω values to be emitted, i.e., to find themselves outside the sphere with R=40 fm. The values in this table were obtained from Fig.7 where the survival probability (eq.8) is plotted as a function of time. This probability tends to a constant value that is non-zero since only a small fraction of the neutrons are emitted during scission. One can see that half of the unbound neutrons are emitted at 3×10^{-21} sec (if Ω=1/2) and at 1.5×10^{-21} (if Ω=9/2). This is the order of magnitude of the 'half-life' of the emission of neutrons at scission.

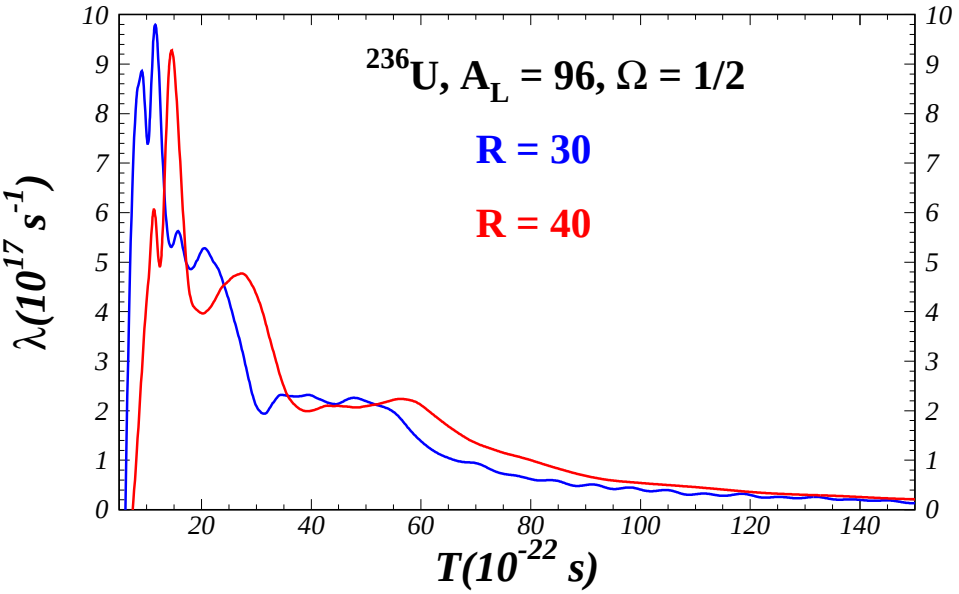

Figure 6: Comparison between the time dependent decay rates calculated on spheres with different radii R.

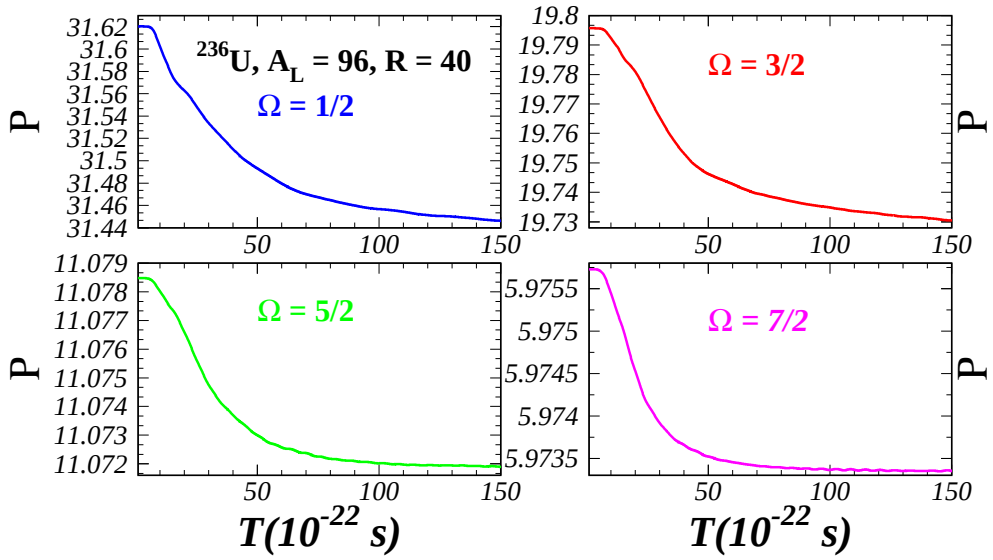

Figure 7: Neutron survival probabilities as a function of time calculated with eq.8 for different values of Ω.

Table 1: Time necessary for 10%,50% and 90% of the scission neutrons to leave the sphere with R=40 fm as a function of Ω.

Ω	$T(10\%)$	$T(50\%)$	$T(90\%)$
1/2	9.9×10^{-22}s	30.2×10^{-22}s	82.2×10^{-22}s
3/2	12.7×10^{-22}s	31.7×10^{-22}s	84.3×10^{-22}s
5/2	11.6×10^{-22}s	27.4×10^{-22}s	60.3×10^{-22}s
7/2	9.4×10^{-22}s	19.9×10^{-22}s	45.1×10^{-22}s
9/2	8.7×10^{-22}s	15.8×10^{-22}s	34.7×10^{-22}s

2.5 The angular distribution

In terms of the emitted part of the wave packet one obtains **the current density**, a vector defined as

$$\bar{J}^i_{em}(\rho, z, T) = \frac{\mathbf{i}}{\hbar}\frac{\hbar^2}{2\mu}(Y\nabla Y^* - Y^*\nabla Y) = J^i_\rho \bar{e}_\rho + J^i_z \bar{e}_z, \tag{10}$$

with $Y = |\Psi^i_{em}\rangle$. From this one calculates **the number of neutrons** that leave a sphere of radius R (around the fissioning nucleus) in a solid angle $d\Omega$ and in a time interval dt is:

$$d\nu^{em}_{sc} = \bar{J}_{em}(R, \theta, t)\bar{n}(R, \theta, t)R^2 dt d\Omega. \tag{11}$$

The angular distribution is given by the integral with respect to t of the above quantity:

$$d\nu^{em}_{sc}/(\sin\theta d\theta) = 4\pi \int_0^T \bar{J}_{em}(R, \theta, t)\bar{n}(R, \theta)R^2 dt. \tag{12}$$

$\bar{n}$ is the unit vector perpendicular to the surface. The upper limit should in principle be ∞. In practice we can reach only a finite value T_{max}. By a further integration with respect to θ ($d\Omega = \sin\theta d\theta$) one obtains **the total number of emitted neutrons** (ν^{em}_{sc}) at T_{max}.

Fig.8 shows the angular distribution with respect to the fission axes of scission neutrons with projection of the angular momentum Ω=1/2 at 4 consecutives times after the neck rupture. The emission takes place mainly along the fission axes with a preference for the direction of the light fragment as in experiment. So the most probable angles are 0° and 180°. Fig.9 shows the drastic change of the angular distribution due to the value of Ω. At Ω=3/2 already, there is no emission at 0° and 180° and this trend accentuates with increasing Ω so that at Ω=9/2 the most probable angle is perpendicular to the fission axes as in the case of charged particles (mainly alpha particles) which accompany the fission process. In this respect the scission neutrons are totaly different from the evaporated neutrons and this difference could be used to distinguish between the two

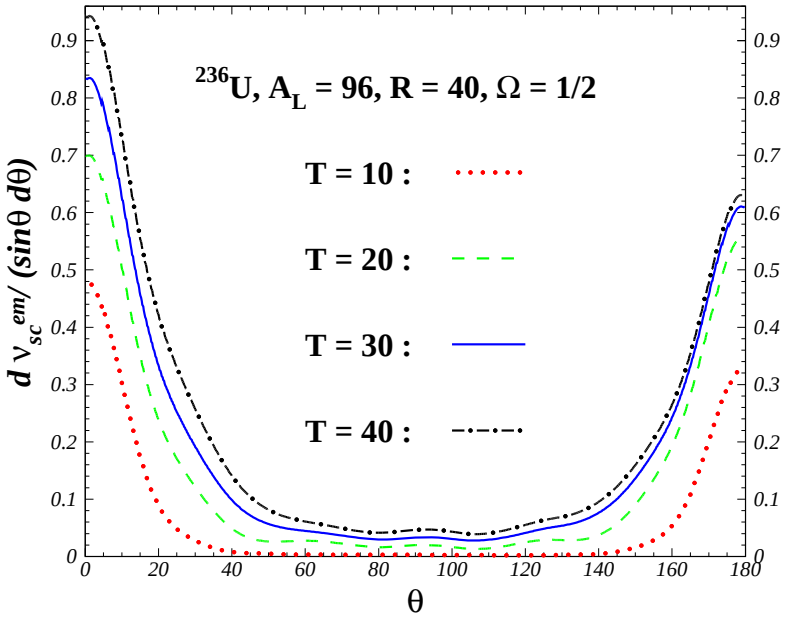

Figure 8: Scission-neutron angular distribution for Ω=1/2 at different times after scission (T is in 10^{-22} s).

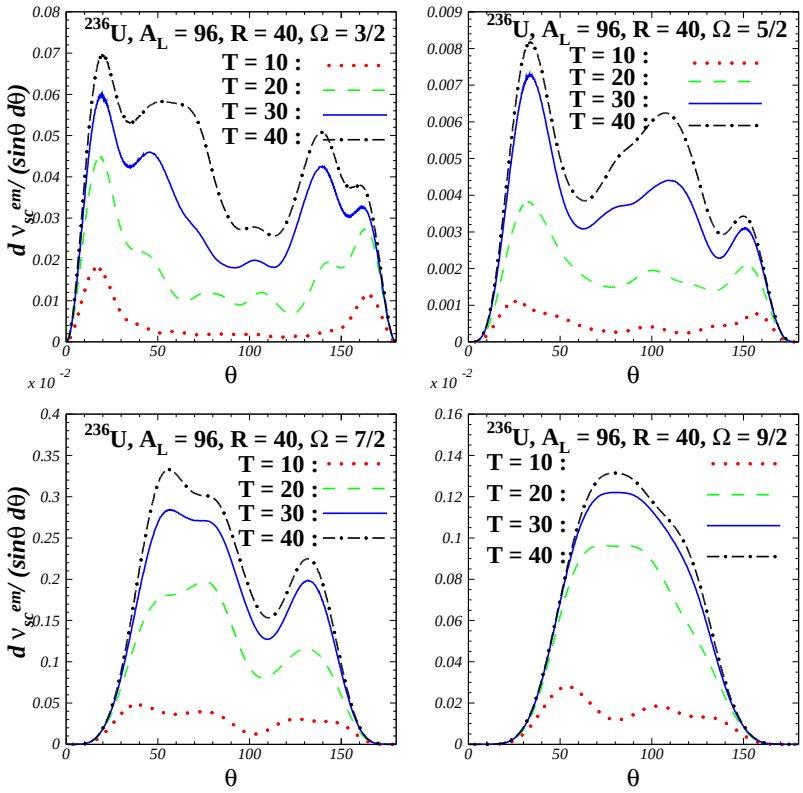

Figure 9: The same as in Fig. 5 but for larger values of Ω

components. The evaporated neutrons are emitted isotropically in the fragments frame. The anisotropy of their angular distribution in the laboratory system is simply due to the kinematics of the post scission separation of the fragments. It has therefore nothing to do with the intrinsic properties of the neutrons (such as Ω).

2.6 The kinetic energy spectra

Fig.10 shows kinetic energy spectra for Ω=1/2, Ω=3/2, Ω=5/2, Ω=7/2 and Ω=9/2 respectively. The kinetic energy increases with increasing Ω due to the centrifugal term. Note however that $\Omega = 1/2$ gives the dominant contribution (65%).

2.7 Conclusions

The decay rate λ of the scission-neutron emission is time dependent. At short times after scission λ(t) oscillates: we are dealing with a pulsed emission. At large times the oscillations are damped and λ tends to an almost constant value: we are dealing with and exponential decay. The transition between these two behaviours depends on the quantum number Ω. From the time dependence of the survival probability N_{int}(t) we deduced the 'half-life' of the scission-neutron emission: $\approx 2.5 \times 10^{-21}$ sec. So the emission starts during the scission process and covers the first part of the fragments acceleration phase.

The angular distribution of the scission neutrons with respect to the fission axes (hence in the laboratory system) was calculated for sets of neutron wavefunctions defined by a given Ω value (1/2, 3/2, 5/2, 7/2 and 9/2). A strong dependence on Ω was found. Namely, wave functions with different Ω have different most probable emission angles: from emission along the fission axes (1/2) to emission perpendicular to the fission axes (9/2). This result leads to a new interpretation of the measured angular distribution of the PFN, completely different from the one provided by the EVN hypotheses. It may open a possibility to separate the two components of the PFN.

Concerning the energy spectrum we note that the SN spectrum presents structures, in qualitative agreement with the measured spectrum.

3 Phase nr. 3 (21/12/2018 - 31/12/2019)

The dependence of the scission neutron multiplicity on the mass ratio of the fission fragments in the case of ^{236}U and ^{252}Cf. The comparison of the results obtained in the frame of the two hypotheses with respect to the origin of the prompt neutrons of fission. The influence of the model parameters: the minimal radius before scission and the distance between the interior surfaces of the fragments after scission.

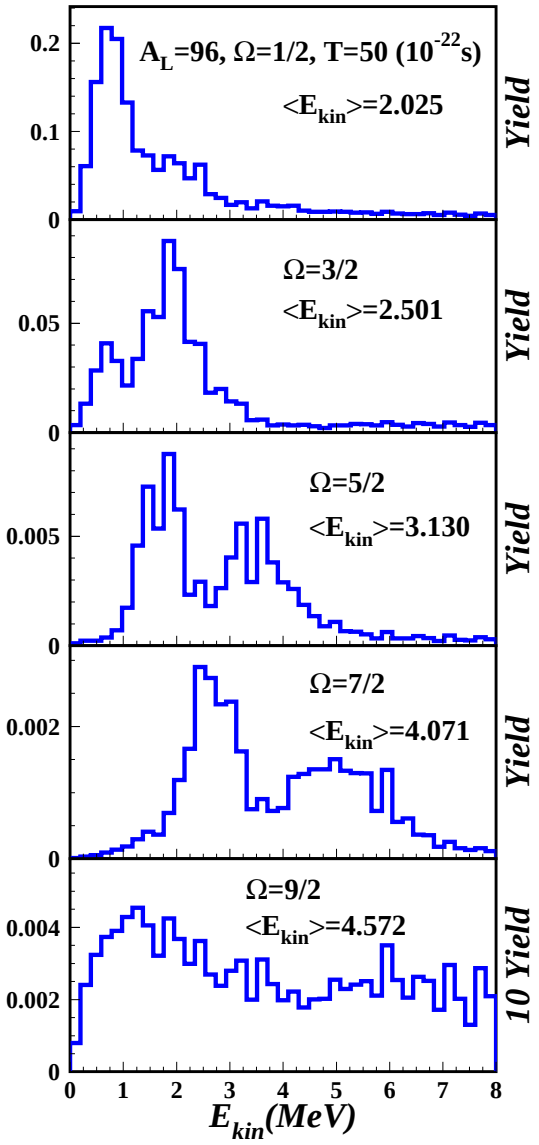

Figure 10: Kinetic energy distributions at $T = 50 \times 10^{-22}$ sec for sub-states defined by the quantum number Ω. $Yield = \sum P_i(E_{kin}) \times v_i^2$.

3.1 Estimated results

-The calculation of the scission neutron multiplicity in terms of A_{Light}/A_{Heavy} in the sudden approximation, which assumes a infinitely short duration of the scission process.

-The calculation of the angular distribution of the evaporated and scission neutrons for a fixed mass ratio in the case of low energy fission of the nucleus ^{236}U.

-There will be established the values of the parameters r_{min} and d_{min} which lead to neutron multiplicities in agreement to the experimental data.

-The comparison of the results with recent measurements of the prompt neutron multiplicities in the reactions $^{235}\mathrm{U}(n_{th}, f)$ and $^{252}\mathrm{Cf}(sf)$.

-The comparison of the results with recent experimental data obtained with improved angular (FWHM=7 deg) and mass (3 amu) resolutions.

-The establishment of the character of the emission process of the scission neutrons: exponential or oscillatory. By knowing the energetic and the angular range at which each set contributes we will select experimentally the neutrons with well defined quantum numbers. This opportunity is unique (no other method exists) - Part II.

3.2 Activities

The comparison of the results with recent measurements of the prompt neutron multiplicities in the reactions $^{235}\mathrm{U}(n_{th}, f)$ and $^{252}\mathrm{Cf}(sf)$.

The analysis of the effects due to the neutrons scattering on the primary fragments and to the re-absorption of the neutrons by the fission fragments.

The optimization of the two parameters of the model.

The study of the competition between the two components of the prompt fission neutrons in the region where the evaporated (EVN) and the scission neutrons (SN) overlap - Part II.

3.3 Introduction

The most important feature of the nuclear fission is that it is accompanied by the emission of prompt neutrons (PFN). Two PFN sources have been considered so far:

1) Neutrons evaporated from fully-accelerated excited fragments (EVN).

2) Neutrons dynamically released at scission (SN) due to the diabatic coupling between the neutron degree of freedom and the rapidly changing neutron-nucleus potential.

It is very difficult to separate EVN and SN experimentally since the gross features of PFN can be accounted for by both hypotheses.

Theoretical approaches, accompanied by the comparison with experimental data, are important tools in clarifying these problems.

In this phase we study the dependence of the scission neutron multiplicity on the mass ratio of the fission fragments in the case of ^{236}U and ^{252}Cf. Also we compare the results obtained in the frame of the two hypotheses with respect to the origin of the prompt neutrons of fission and investigate the influence of the model parameters: the minimal radius before scission and the distance between the interior surfaces of the fragments after scission.

3.4 Evaporation model (EVM)

The calculations with the evaporation model is based on the CGMF code [9] which is a Monte Carlo implementation of the well-known Hauser-Feshbach statistical theory of nuclear reactions, applied to the de-excitation of the fission fragments. In its current version, CGMF assumes that there is no pre-scission neutron emission, except at higher energies in the multi-chance fission process, and that all neutron and γ-ray evaporations happen only after the two complementary fragments reach full acceleration. The mean excitation energy of the fission fragments in low-energy fission reactions is typically 15 to 20 MeV. At those excitation energies, only neutron and γ evaporations are allowed, light-charged particle emissions being hindered by the Coulomb barrier. The fragments will spend most of their excitation energy through neutron evaporation, followed by γ-ray decays until a ground or isomeric state is reached.

According to the Hauser-Feshbach theory, the decay of an excited compound nucleus, here a fission fragment, is governed by emission probabilities. The emission probability of a neutron of energy ϵ_n from an initial nucleus (Z, A) characterized by an energy U_i, spin J_i, and parity π_i is given by

$$P_n(\epsilon_n)d\epsilon_n \propto T_n(\epsilon_n, l, j)\rho(A-1, Z, U_f, J_f, \pi_f)d\epsilon_n, \tag{13}$$

the final energy in the residual nucleus given by $U_f = U_i - \epsilon_n - B_n$, final spin J_f and final parity π_f. The neutron transmission coefficients $T_n(\epsilon_n, l, j)$ are obtained as usual from optical model calculations of the neutron+residual nucleus interaction. Spin and parity selection rules are applied at each stage of the decay. The level density ρ entering in Eq. 13 is a short-cut notation to describe a set of discrete excited states at low energies, followed by a continuum representation at higher energies, where individual states cannot be distinguished anymore. Known nuclear levels for the fission fragments are taken from the RIPL-3 database [10]. Nuclear level density parameter systematics are also taken from RIPL-3. Prompt γ-ray emission probabilities are obtained similarly as

$$P_\gamma(\epsilon_\gamma)d\epsilon_\gamma \propto T_\gamma(\epsilon_\gamma)\rho(A, Z, U_f, J_f, \pi_f)d\epsilon_\gamma, \tag{14}$$

with $U_f = U_i - \epsilon_\gamma$.

As mentioned earlier, CGMF uses the Monte Carlo technique to perform this calculation. At each stage of the decay, characterized by a specific nucleus in a specific energy, spin and parity configuration, CGMF calculates the neutron and γ emission probabilities, and then sample those. In this way, different decay paths are generated at each

new CGMF run. By performing a large number of CGMF computations, "histories" of fission events can be recorded, similarly to what is done with list-mode data acquisition in modern experiments.

The outcome of any evaporation model depends on the partition of the total excitation energy among the light and the heavy fragment which is unknown. It is usually parametrized by the ratio T_L/T_H of the fragments' temperatures. In the present calculations we use the assumption of thermal equilibrium [11].

3.5 Dynamical scission model (DSM)

While the EVN depend on the excitation and extra deformation with which the fission fragments are born [11], the SN depend on the dynamical evolution of the system during the scission process [1, 2]. There are three parameters in the dynamical scission model: the nuclear shapes just before (α_i) and immediatelly after (α_f) scission and the duration ΔT of the transition between these two shapes. The shapes are described by Cassini ovals [12]. To simulate the evolution of the neutron wave functions from α_i to α_f lasting ΔT, the two-dimensional time-dependent Schrödinger equation (TDSE2D) with a time-dependent potential (TDP) is solved. The distribution of final wave packets $\hat{\Psi}^i(\Delta T)$ (that correspond at $t = 0$ to the eigenstates $\hat{\Psi}^i$ of α_i) over the eigenstates $\hat{\Psi}^f$ of α_f:

$$a_{if} = \langle \hat{\Psi}^i(\Delta T) | \hat{\Psi}^f \rangle. \tag{15}$$

constitutes the core of DSM. All wave functions have an implicit dependence on the cylindrical coordinates (ρ, z). a_{if} is $\neq 0$ only if $|\hat{\Psi}^i\rangle$ and $|\hat{\Psi}^f\rangle$ have the same projection Ω of the total angular momentum along the symmetry axis. The rapid change of the potential in which the nucleons move produces, by means of a diabatic coupling, their excitation and eventual emission. The a_{if} coefficients are used to calculate the scission neutron multiplicity ν_{sc} in a simple and intuitive way. It is given by the sum of the probabilities P^i_{em} that a neutron occupying a given bound-state i is emitted:

$$\nu_{sc} = 2 \sum_i P^i_{em}, \qquad P^i_{em} = v_i^2 \left(\sum_f |a_{if}|^2 \right) \tag{16}$$

i-sum is over bound states while f-sum is over unbound states. v_i^2 is the occupation probability of the state i.

3.6 Results

3.6.1 The scission neutron multiplicity in the sudden approximation

The sudden approximation assumes that fission motion is adiabatic until the neck rupture at finite radius and that this rupture is followed by a sudden absorption of the neck pieces by the fragments. We are therefore dealing with a transition between two different nuclear configuratios ($\alpha_i \rightarrow \alpha_f$) and we only need to know the corresponding two

sets of bound-neutron eigenstates. These are calculated from the bi-dimensional stationary Schrödinger equation and are characterized by the projection Ω of the angular momentum on the symmetry axis.

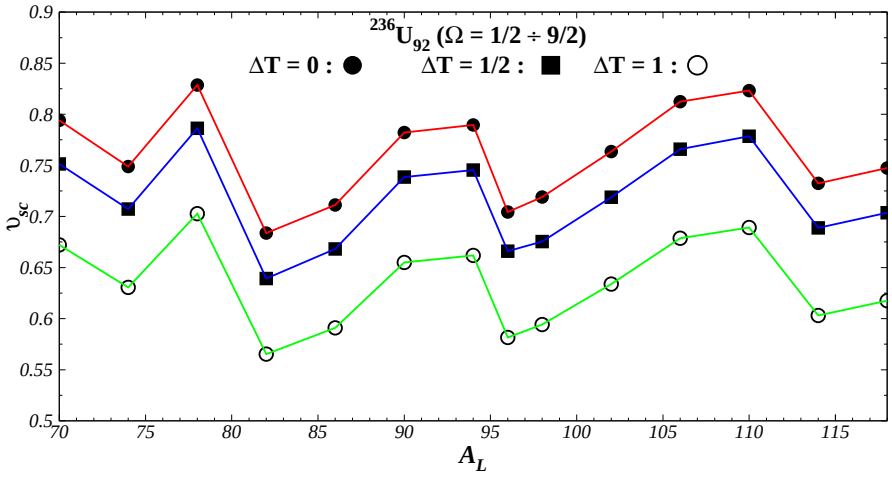

Figure 11: Scission neutron multiplicity as function of light-fragment mass

In Fig.11 the multiplicities for ^{236}U are presented with the sudden approximation ($\Delta T = 0$) and with two values of $\Delta T > 0$ (the dynamical model). The sudden values are upper limits of the multiplicities.

3.6.2 The angular distribution of the evaporated and scission neutrons for a fixed mass ratio

1) The Hauser-Feshbach Monte-Carlo technique described in Sect. 3.4 is applied to the de-excitation of each of the two fragments by isotropic emission of neutrons and γ-rays. The two fragments are supposed to have the same temperature. A transformation from the CM system of each fragment to the LAB system is finally performed.

The corresponding angular distributions of the evaporated neutrons for four mass divisions chosen around the most probable one ($A_L/A_H = 96/140$) are presented in Fig.12.

The comparison with experimental data [6] is included.

2) By Eq.12 from DSM we calculate the angular distribution for fixed mass ratios defined by the mass of the light fragment A_L. It is then convoluted with a Gaussian resolution function. The results for $A_L = 90, 94, 96, 98$ are compared in Fig.13 with the mentioned measurements [6].

Two features are worth mentioning:

a) In the range (40° - 140°) the data reveal structures that could be due to scission-neutron scattering on nascent fragments.

b) In the direction of the fragments (i.e., in the ranges (0° - 40°) and (140° - 180°) the

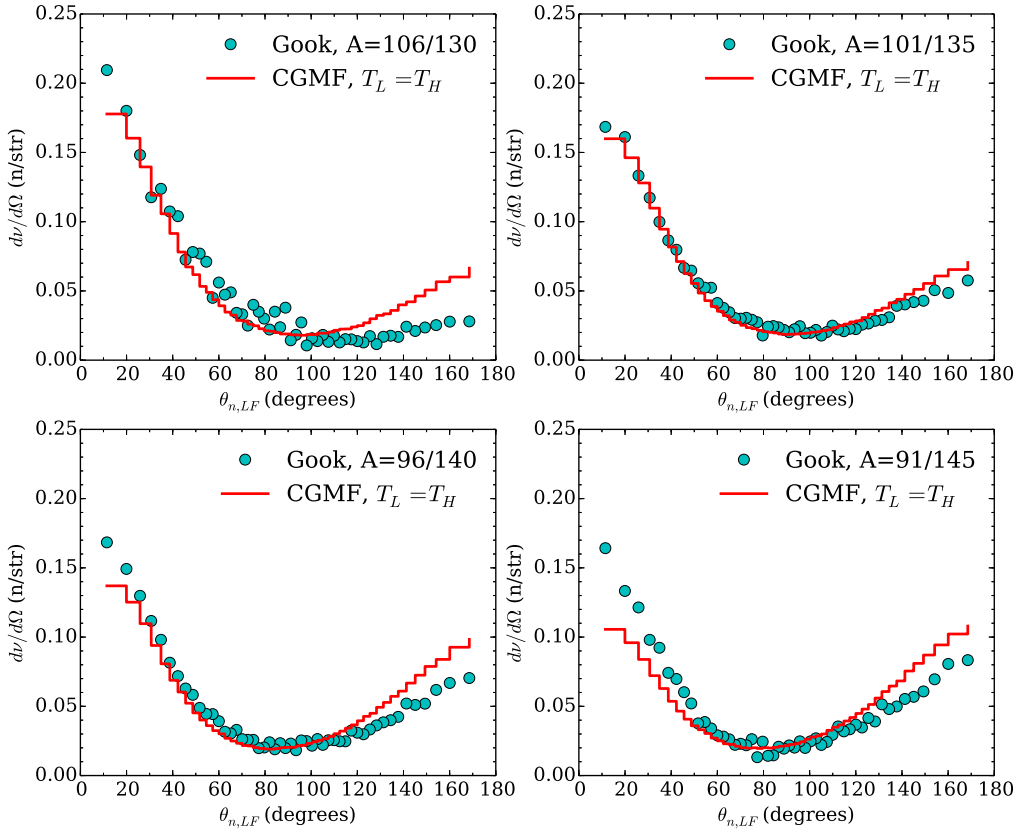

Figure 12: Angular distribution with respect to the light-fragment direction calculated with CGMF for selected fragment-mass ratios.

distribution is rather flat. It is flatter on the heavy fragment side. This could be a sign of scission-neutron reabsorption by the fission fragments with the heavy fragment having a stronger effect.

The reabsorption of the scission neutrons can be better simulated by introducing a complex potential in the TDSE2D. Fig.14 shows the effect of the imaginary potential on the SN angular distribution. As expected it reduces the scission neutron flux in the direction of the fragments while the neutrons moving perpendicular to the fission axes are unaffected.

3.6.3 The values of the parameters r_{min} and d_{min} which lead to neutron multiplicities in agreement to the experimental data.

The last four rows of Table 2 contain the calculated contributions of the L and of the H fragments to the SN multiplicity at different times T after scission. They represent

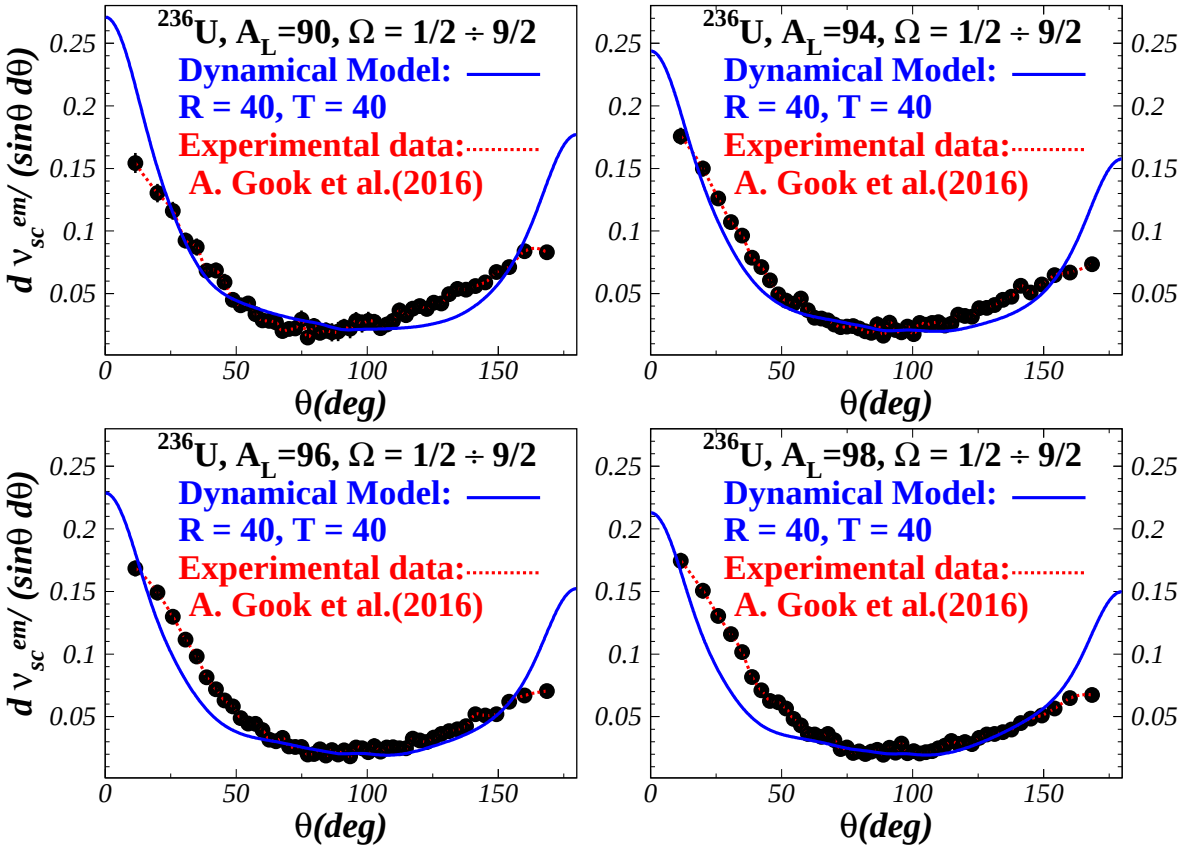

Figure 13: Angular distribution with respect to the light-fragment direction calculated with DSM for selected fragment-mass ratios around $A_L/A_H = 96/140$.

neutrons that have crossed the sphere of radius R and move left and right to a plane at 90° to the fission axis. They are calculated by the integral of Eq.(12) with respect to the solid angle. The contributions from the L- and H- fragments are estimated using the prescription from Ref.[14]. A ratio ν_L^{em}/ν_H^{em} close to the experimental value (1.41) [13] is obtained. We get this result with the configuration parameters $\alpha_i = 0.985$ and $\alpha_f = 1.001$ that correspond to $r_{min} = 1.6$ fm (the minimum neck-radius) and $d_{min} = 0.6$ fm (the distance between the surfaces of the two fragments along the z-axis). The duration of the scission process was $\Delta T = 10^{-22}$ sec.

We also studied the dependence of the SN multiplicity, Eq.(16), on the scission configurations involved.

The transition ($\alpha_i = 0.985 \rightarrow \alpha_f = 1.001$) that corresponds to r_{min}=1.6 fm and d_{min}=0.6 fm, used so far, is compared with the transition ($\alpha_i = 0.975 \rightarrow \alpha_f$=1.010) corresponding to r_{min}=1.9 fm (the theoretically predicted value [15]) and d_{min}=2.0 fm. An intermediate configuration ($\alpha_i = 0.980 \rightarrow \alpha_f$=1.005) is also included. The results are presented in Table 3 for the most probable mass division (A_L=96) and two transition times ΔT. As expected, ν_{sc} decreases with increasing ΔT. There is also a strong sensitivity of ν_{sc} on (r_{min}, d_{min}).

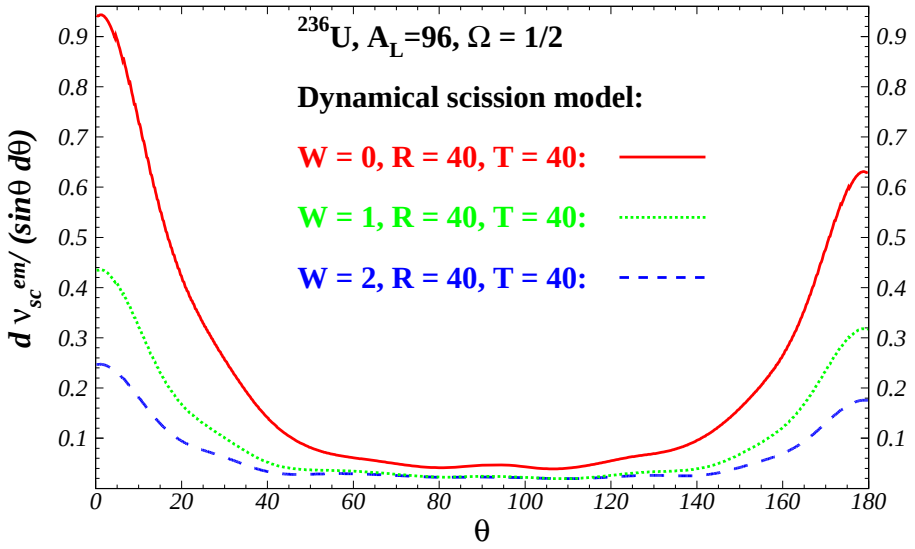

Figure 14: Effect of the complex potential (W(MeV) = Imag(Pot)) on the angular distribution calculated with DSM.

A similar analysis has been performed for the spontaneous fission of ^{252}Cf (with mass asymmetries 109/143 and 112/140 - see Tables 4, 5.

In the Table 6 the evolution of the ratio ν_L^{em}/ν_H^{em} is shown for $A_L = 112$ and $\Delta T = 1$.. A value close to the experimental value (1.21) is obtained, but after a longer time than in the case of ^{236}U.

3.6.4 The comparison with measurements of the prompt neutron multiplicities in the reactions ^{235}U(n_{th}, f) and ^{252}Cf(sf)

.

The calculated multiplicities have been obtained with the occupation probabilities v_i^2 defined either in the hypothesis of particle correlated (BCS) or in the hypothesis of independent particles (IND) [14] - see Figs.15 and 16.

In the case of ^{236}U the represented multiplicities correspond to the sudden approximation. As shown in Fig.11 the multiplicities given by the Dynamical Model are equally shifted below the sudden values.

3.6.5 The comparison of the results with recent experimental data

Our angular distributions were compared with recent experimental data ([6]), that used improved angular (FWHM=7 deg) and mass (3 amu) resolutions, in Figs.12 and 13 from Section 3.6.2. Also, the kinetic energy spectra has been compared with measured data, as will be shown in the next section.

Table 2: Total number of neutrons (ν_{sc}^{em}) (for ^{236}U and $A_L = 96$) that crossed the spheres of $R = 30$ and 40 fm at succesive time intervals T. The ratio of the contributions from the L and H fragments is also included. All times are in 10^{-22} sec.

A_L	$96(R = 30)$		$96(R = 40)$	
T	ν_{sc}^{em}	ν_L^{em}/ν_H^{em}	ν_{sc}^{em}	ν_L^{em}/ν_H^{em}
10	0.118	1.424	0.043	1.562
20	0.258	1.348	0.152	1.256
30	0.363	1.402	0.247	1.281
40	0.429	1.414	0.320	1.407

Table 3: Dependence of ν_{sc} (for ^{236}U with A_L=96) on (r_{min}, d_{min}) in fm and on ΔT.

ΔT \ $r_{min}(d_{min})$	1.6 (0.6)	1.7 (1.8)	1.9 (2.0)
1×10^{-22} sec	0.551	1.393	2.538
2×10^{-22} sec	0.385	1.004	1.887

3.6.6 The establishment of the character of the emission process of the scission neutrons: exponential or oscillatory. The energetic and the angular range - Part II

In the previous phase we have studied the time-dependent decay rate, showing that it has an oscillatory behaviour immediately after the neck rupture, while with increasing time the amplitude of these oscillations diminishes and asymptotically reaches an almost constant value indicative of an exponential decay.

The angular distribution with both types of neutrons (EVN and SCN) has been discussed in Section 3.6.2.

In the following we present some new relevant results concerning the energetic spectrum. First, we recall the total energy spectrum (summed over Ω values from 1/2 to 9/2) which is given as histogram in Fig.4. It exhibits a maximum around 0.7 MeV and an exponentially decreasing tail until 8 MeV in qualitative agreement with the measured spectrum [5] of all prompt fission neutrons (PFN).

One notices that both the data and the calculation are not smooth. The oscillations in the data are statistically significant. The calculated distribution is not smooth since it consists of a finite weighted sum of individual contributions with different mean values and widths. The number of non-negligible terms is only 35, distributed among the Ω values as following: 21 for 1/2, 8 for 3/2, 4 for 5/2 and 2 for 7/2. Hence less than half of the total number of the neutrons in ^{236}U contribute significantly to the scission

Table 4: Dependence of ν_{sc} (for ^{252}Cf with $A_L = 109$) on (r_{min}, d_{min}) in fm and on ΔT.

ΔT \ $r_{min}(d_{min})$	1.6 (0.6)	1.9 (2.0)
1×10^{-22} sec	0.763	3.318
2×10^{-22} sec	0.550	2.511

Table 5: Dependence of ν_{sc} (for ^{252}Cf with $A_L = 112$) on (r_{min}, d_{min}) in fm and on ΔT.

ΔT \ $r_{min}(d_{min})$	1.6 (0.6)	1.9 (2.0)
1×10^{-22} sec	0.600	2.798
2×10^{-22} sec	0.421	2.078

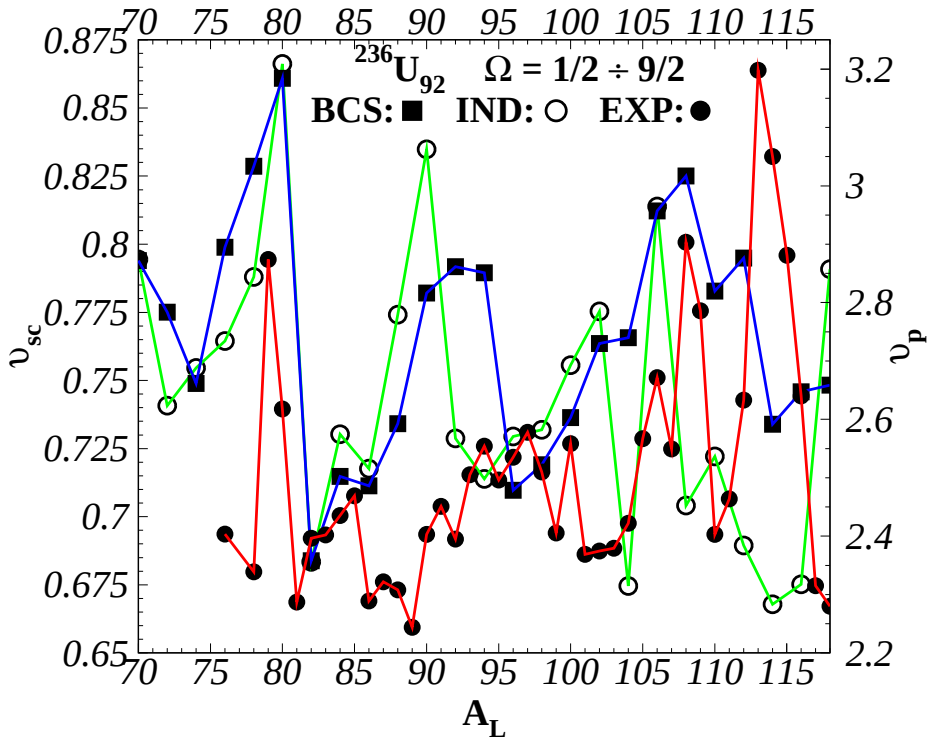

Figure 15: Scission neutron multiplicity as function of light-fragment mass vs. measured prompt neutron multiplicities for ^{236}U.

neutron spectrum.

However the data do not oscillate as much as the calculations. One reason is that the data are affected by a finite energy resolution. If we convolute the theoretical spectrum with a Gaussian resolution function, the amplitude of its oscillations will decrease. This is shown in Fig.17 where a resolution between 0.3 and 0.4 MeV brings the amplitude

Table 6: Total number of neutrons (ν_{sc}^{em}) (for ^{252}Cf and $A_L = 112$) that crossed the sphere of radius $R = 30$ fm at succesive time intervals T. The ratio of the contributions from the L and H fragments is also included. All times are in 10^{-22} sec.

A_L	$112(R = 30)$	
T	ν_{sc}^{em}	ν_L^{em}/ν_H^{em}
30	0.342	1.072
40	0.383	1.108
50	0.411	1.127
60	0.431	1.155
80	0.458	1.196
100	0.477	1.218

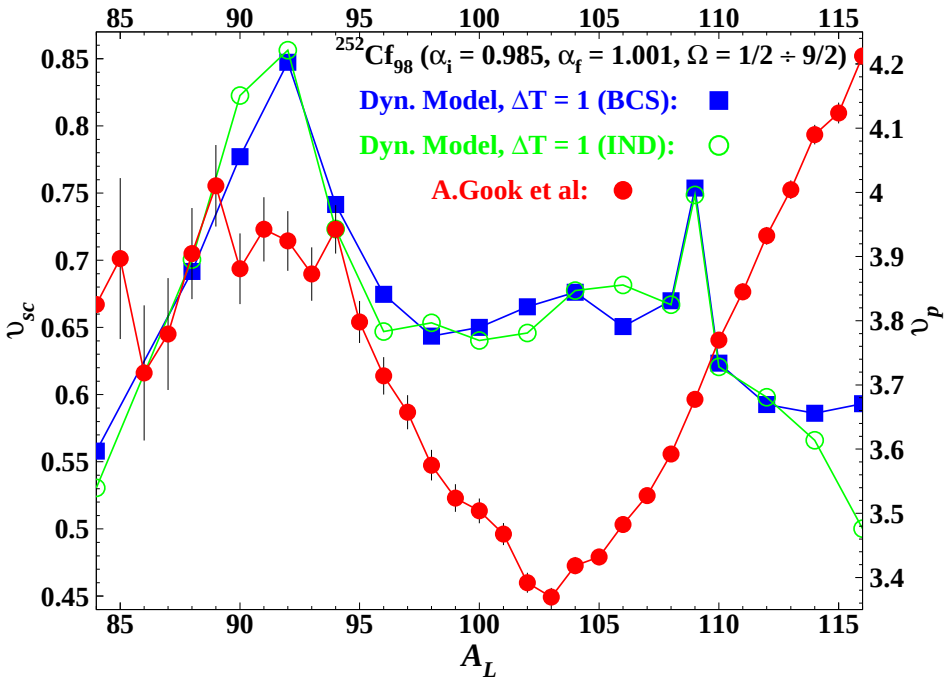

Figure 16: Scission neutron multiplicity as function of light-fragment mass vs. measured prompt neutron multiplicities for ^{252}Cf.

of the oscillations into better agreement. This is however not the only reason. There is also the finite fragment-mass resolution and the fact that our model (as does any model) contains approximations and numerical limitations.

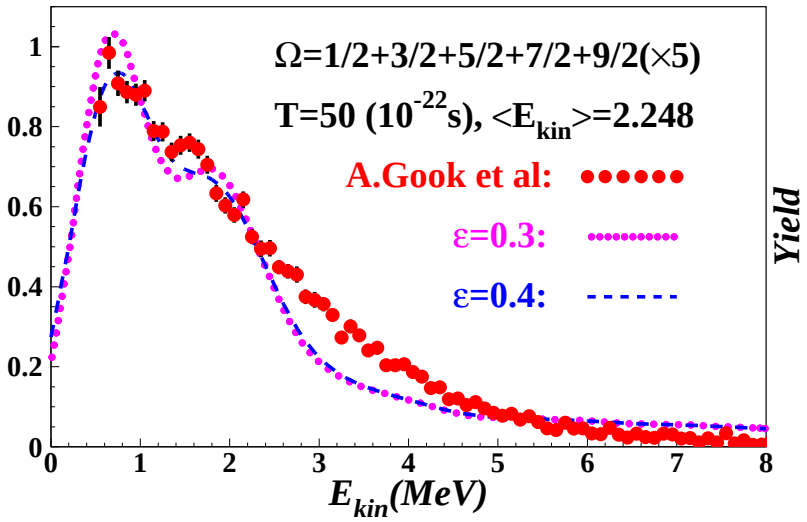

Figure 17: The SN spectrum convoluted with Gaussian resolution functions with half-width equal 0.3 and 0.4 MeV

3.7 Conclusions

1. Calculations have been performed for the reaction $^{235}U(n_{th}, f)$. The scission neutron multiplicity depends on the transition time ΔT: longer the time lower the multiplicity. A precise knowledge of ΔT is therefore necessary. In addition it depends on r_{min} and d_{min} that characterize the transition at scission. We found that the parameters of the model (transition $0.975 \rightarrow 1.010$ and $\Delta T = 10^{-22}$ sec) leads to the optimal agreement with the experimental data.

2. Deviation between the calculated and measured angular distribution are noticed for angles larger than 100° with respect with the light fragment direction; calculations overestimated data. It is a sign of neutron reabsorption by the fragment, mainly by the heavy one. This effect is studied quantitatively by introducing an imaginary part in the neutron-nucleus potential.

3. The existing structures in the data in the angular domain $[40°, 140°]$ are interpreted as due to the scattering of the scission neutrons on the nascent fragment (rainbow scattering).

4. In the case of spontaneous fission of ^{252}Cf, the calculated ratio ν^L_{em}/ν^H_{em} (1.21) is again close to the experimental value (1.22).

5. The kinetic energy distribution of the scission neutrons has been also calculated and compared with the total prompt fission neutron measured spectrum. The histogram of the kinetic energy distribution (summed over all Ω values) has a maximum at 0.7 MeV and an exponentially decreasing tail until 8 MeV, in qualitative agreement with the data. In addition, both the data and the calculations are not smooth but present statistically significant oscillations that we interpret as being due to a relatively small number of neutrons that contribute.

N.B. Toate activităţile propuse au fost realizate integral în conformitate cu planul de realizare. Pentru întreaga perioadă au fost publicate 5 lucrări cu acknowledgment la proiectul PN-III-P4-ID-PCE-2016-0649 (Contract No. 194/2017).

PUBLICATIONS IN THE FRAME OF THE PROJECT

[1] Parallel theoretical study of the two components of the prompt fission neutrons: dynamically released at scission and evaporated from fully accelerated fragments, N.Carjan, M.Rizea, P.Talou, EPJ Web of Conferences 146, art.no.04002, p.1-6 (2017)

[2] Fourier transform of single-particle wave functions in extremely deformed nuclei: towards the momentum distribution of scission neutrons, M.Rizea, N.Carjan, EPJ Web of Conferences 169, art.no.00020 (2018)

[3] Charge polarization and the elongation of the fissioning nucleus at scission, C.Ishizuka, S.Chiba, N.Carjan, Romanian Reports in Physics 70, 202 (2018)

[4] Structures in the energy distribution of the scission neutrons: finite neutron-number effect, N.Carjan, M.Rizea, Physical Review C 99, 034613 (2019)

[5] Fission of superheavy nuclei: Fragment mass distributions and their dependence on excitation energy, N.Carjan, F.A.Ivanyuk, Yu.Ts.Oganessian, Physical Review C 99, 064606 (2019)

References

[1] M. Rizea, N. Carjan, Nuc. Phys. A **909**, 50–68 (2013)

[2] N. Carjan, M. Rizea, Phys. Lett. B **747**, 178–181 (2015)

[3] M. Rizea, N. Carjan, Eur. Phys. J. A **52**, 368 (2016)

[4] W.H. Press, B.P. Flannery, S.A. Teukolsky,W.T. Vetterling, *Numerical Recipes* (Cambridge Univ. Press, 1996) 451–453

[5] N. Kornilov, F.-J. Hambsch et al., Nucl. Sci. Eng. **165**, 117–127 (2010).

[6] A. Göök, F.-J. Hambsch, W. Geertz, M. Vidali, private communication.

[7] A. Göök, F.-J. Hambsch, S. Oberstedt, Theory-4 Workshop (2017), Varna, Bulgaria, EPJ Web of Conferences **169**, 00004 (2018).

[8] J. M. Blatt, V. F. Weisskopf, *Theoretical Nuclear Physics* (John Wiley, New York, 1958) 368.

[9] P. Talou, T. Kawano, I. Stetcu, CGMF User Manual, Los Alamos Technical Report, LA-UR-14-24031.

[10] R. Capote et al., Nuclear Data Sheets **110**, 3107 (2009).

[11] D.G. Madland, J.R. Nix, Nucl. Sci. Eng. **81**, 213 (1982).

[12] V. Pashkevich, Nucl. Phys. A **169**, 275 (1971).

[13] K. Nishio et al., Nucl. Phys. A **632**, 540 (1998).

[14] N. Carjan, F.-J. Hambsch, M. Rizea, O. Serot, Phys. Rev. C **85**, 044601 (2012).

[15] F. A. Ivanyuk, K. Pomorski, Phys. Rev. C **79**, 054327 (2009).

Project director,

Dr. Nicolae Carjan